

The physical conditions in Gomez’s Hamburger (IRAS 18059-3211), a pre-MS rotating disk[★]

V. Bujarrabal¹, K. Young², and A. Castro-Carrizo³

¹ Observatorio Astronómico Nacional (OAN-IGN), Apartado 112, 28803 Alcalá de Henares, Spain
e-mail: v.bujarrabal@oan.es

² Harvard-Smithsonian Center for Astrophysics, 60 Garden Street, Cambridge, MA 02138, USA
e-mail: rtm@cfa.harvard.edu

³ Institut de RadioAstronomie Millimétrique (IRAM), 300 rue de la Piscine, 38406 St. Martin d’Hères, France
e-mail: ccarrizo@iram.fr

Received 27 October 2008 / Accepted 2 February 2009

ABSTRACT

Aims. We aim to study the structure, dynamics, and physical conditions of Gomez’s Hamburger (IRAS 18059-3211; GoHam), and in particular confirm that GoHam mainly consists of a flaring disk in Keplerian rotation around a young, probably pre-MS star.

Methods. We present high resolution SMA maps of $^{12}\text{CO } J=2-1$, $^{13}\text{CO } J=2-1$, $^{12}\text{CO } J=3-2$, and $\text{C}^{17}\text{O } J=3-2$, as well as data on $^{12}\text{CO } J=6-5$ and the continuum flux at these wavelengths. Spatial resolutions as high as $1''$ are attained. Except for the C^{17}O data, the dynamical ranges are larger than 10. The maps are compared with a numerical model, which simulates the emission of a rotating disk with the expected general properties of such objects, and a very satisfactory fitting of our maps is obtained. The meaning and reliability of our results are thoroughly discussed.

Results. Our observations allow measurement of the main properties of GoHam on scales of between $\sim 1''$ ($\sim 5 \times 10^{15}$ cm, for the assumed distance, 300 pc) and the total extent of the nebula, $14''$. We are able to measure the global structure of the gas-rich disk, which is found to be flaring, and its dynamics, which is clearly dominated by Keplerian rotation, with a small degree of turbulence. The combination of different lines, in particular of different opacities, allows us to estimate reasonably the distributions of gas temperature and density. We clearly find a significant and sharp increase in temperature at large distances from the equator, accompanied by a decrease in density of the same order. Finally, we identify a condensation in the southern part of the disk that has no counterparts in the northern nebula. This condensation is quite extended (about 5×10^{15} cm), contains a significant amount of mass (roughly, $\sim 6 \times 10^{-3} M_{\odot}$), and seems to be associated with a detectable distortion of the global rotation kinematics. We discuss several possible interpretations of that feature.

Key words. stars: circumstellar matter – stars: planetary systems: protoplanetary disks – stars: formation – stars: individual: Gomez’s Hamburger

1. Introduction

Originally identified on a plate by A. Gómez in 1985, Gomez’s Hamburger (IRAS 18059-3211; hereafter GoHam) is a very interesting nebula that remains poorly studied. It has a spectacular optical image (see Ruiz et al. 1987; Bujarrabal et al. 2008, and HST images in press release number 2002-19), in which a dark lane of dust separates two flat, bright regions, presumably illuminated by a central star that remains hidden by the equatorial disk. From spectroscopic analysis of the scattered light (Ruiz et al. 1987), the central star was classified as an A0-type star. GoHam’s spectral energy distribution (SED) exhibits two maxima, in the optical and FIR (Ruiz et al. 1987), which correspond respectively to the stellar emission scattered by the bright lobes and to radiation re-emitted by dust grains in the dark equatorial region.

GoHam was originally proposed to be a post-AGB nebula (Ruiz et al. 1987). However, high-resolution CO maps (Bujarrabal et al. 2008, hereafter, Paper I) were used to demonstrate that the nebula is almost exactly in Keplerian rotation, around the symmetry axis clearly identifiable in its image.

No component other than the rotating, flaring disk, at least on the large scale probed by the arcsec resolution attainable with mm-wave interferometry, seems to be present in the nebula. Bujarrabal et al. (2008) estimated the central (presumably stellar) mass and concluded that, for any possible distance, its high value in combination with the relatively low total luminosity of the source is incompatible with the idea that GoHam is an evolved object. These authors concluded that Gomez’s Hamburger is very probably a pre-main-sequence object at a much smaller distance than previously believed, of 500 pc, although this value remains uncertain. Wood et al. (2008) developed a model of dust emission and scattering that can explain the optical and IR SED for a distance of about 300 pc. The total disk mass determined by these authors, $0.3 M_{\odot}$, is similar to that deduced in Paper I from a simple analysis of the mm-wave dust emission (taking into account the different distances assumed in these papers), and is probably dominated by the dense inner regions. Berné et al. (2009) also suggested a distance of about 200–300 pc, arguing that the spectral type could be slightly less early than that obtained by Ruiz et al. (1987). The determination of the distance is based on the comparison of several observational parameters obtained in GoHam with theoretical evolutionary tracks and previous data for other young

[★] Appendix A is only available in electronic form at <http://www.aanda.org>

stars. The relevant parameters are: the total luminosity (obtained from integration of the SED, but dependent on the anisotropy of the dust-processed radiation, see below), the central mass (from the nebula rotation), and the stellar surface temperature (see discussion on the stellar type accuracy by Berné et al. 2009). If the stellar type is slightly less early than proposed by Ruiz et al. (1987), a distance of about 300 pc is consistent with all existing data. These smaller values of distance yield a slightly smaller linear radius for the disk, in closer agreement with results found for similar objects. We accordingly adopt a distance of 300 pc.

The SED observations of GoHam are quite complete (Ruiz et al. 1987), but the estimate of the luminosity requires us to introduce significant corrections due to the extreme viewing angle of the source and the strong disk opacity at short wavelengths (see Paper I). For the distance assumed here, we can expect a luminosity of $\sim 15 L_{\odot}$ with an uncertainty of about a factor 2. A comparison of this luminosity with pre-MS evolutionary tracks (see van den Ancker et al. 1998, and Paper I) infers a stellar mass of about $2 M_{\odot}$. This value is relatively low compared to the mass derived from the disk rotation curve, $\sim 3 M_{\odot}$, suggesting a significant contribution to the central mass of the innermost disk or even of a low-mass stellar companion (see further discussion in Paper I). We will review in Sect. 4 the nature of the central star(s), taking into account our new results.

Bujarrabal et al. (2008) presented only $^{12}\text{CO } J=2-1$ maps obtained with the SMA, together with a preliminary modeling of the data. The development of these models was limited significantly by the small amount of available data. In particular, the high optical depth expected in this line prevented any accurate determination of the gas density distribution. A significant revision of some parameters tentatively discussed by Bujarrabal et al. (2008) was therefore necessary. In this paper, we also present maps of $^{13}\text{CO } J=2-1$, $^{12}\text{CO } J=3-2$, and $\text{C}^{17}\text{O } J=3-2$. The combination of the $^{12}\text{CO } J=2-1$ line (reanalyzed for this work) with the ^{13}CO and C^{17}O lines, which are optically thin, and the $J=3-2$ emissions, which require significantly more excitation, has allowed a detailed modeling of the source. We now propose realistic distributions on large scale of the gas density and temperature in Gomez’s Hamburger, distributions that, as we will show, appear consistent with theoretical ideas about the properties of passive flaring disks in Keplerian rotation.

2. Observations

We present observations of the $^{12}\text{CO } J=2-1$ (230.5 GHz), $^{13}\text{CO } J=2-1$ (220.4 GHz), $^{12}\text{CO } J=3-2$ (345.8 GHz), and $\text{C}^{17}\text{O } J=3-2$ (337.1 GHz) lines in Gomez’s Hamburger (IRAS 18059-3211, GoHam), obtained with the Submillimeter Array (SMA). We also observed $^{12}\text{CO } J=6-5$ (691.5 GHz), but did not detect the line emission. Both ^{12}CO and $^{13}\text{CO } J=2-1$ were observed simultaneously in 2006. Details of the observations, calibration, and data reduction for these lines may be found in Bujarrabal et al. (2008, Paper I). The reduction of the $^{12}\text{CO } J=2-1$ data set was repeated after the observations were presented in Paper I. The continuum flux at $\lambda = 1.3$ mm was measured to be 0.3 Jy.

The 345 GHz and 690 GHz data were acquired on the night of 2007 March 21 (UT), when the array was in the “Compact North” configuration, a low resolution configuration with longer north-south baselines intended to produce almost circular synthesized beams for low declination sources. Seven of the SMA’s eight antennas were usable in the 345 GHz band, and six were usable in the 690 GHz band. The 345 GHz receivers were tuned

to position the $^{12}\text{CO } J=3-2$ line at 345.796 GHz in the receivers’ upper sideband (USB) and the $\text{C}^{17}\text{O } J=3-2$ line at 337.061 GHz in the lower sideband (LSB). The 690 GHz receivers were tuned to position $^{12}\text{CO } J=6-5$ at 691.473 GHz in the USB. The J2000 coordinates used for GoHam were RA = 18:09:13.37, Dec = $-32:10:49.5$, and correspond to the central cross in our images. Observations began at 11:00 UT and finished at 21:10 UT. During that period, the precipitable water vapor above Mauna Kea varied between 0.6 and 1.0 mm. As the source transited at an elevation of 38 degrees, the double sideband (DSB) system temperature (T_{sys}) of the seven 345 GHz receivers ranged from 133 K to 235 K, while T_{sys} ranged from 1600 K to 2300 K for the 690 GHz receivers. The correlator was configured to have a uniform resolution of 812.5 kHz per channel across the full 2 GHz (DSB) bandpass of each receiver. This resolution is equivalent to 0.70 km s^{-1} for the $J=3-2$ lines, and 0.35 km s^{-1} for the $J=6-5$ line. Observations of Ganymede (16.5 degrees from the source) and the quasar 1924-292 (15.7 degrees from the source) were completed every half hour for calibration of the instrument’s complex gain. To provide bandpass calibration, Saturn and 3C 273 were observed before the source rose.

The data were calibrated with the MIR package. For the 345 GHz data, cross-correlation observations of Saturn, 3C 273 and Ganymede were used in deriving antenna-based bandpass data to correct for the instrument’s spectral response. Ganymede was used for flux calibration, and the derived 850 micron flux for 1924-292 was 2.5 Jy. There were no phase jumps in the data, and complex gain calibration was completed by fitting a 5th order polynomial to the amplitude and phase of the quasar data. The source was tracked between hour angles of -3.5 and $+3.5$ h, and the total on-source integration time was 4 h. Projected baseline lengths ranged from 9.1 to 136 kilolambda. The ^{12}CO and $\text{C}^{17}\text{O } J=3-2$ spectral lines were clearly detected, as was the 850 micron (345 GHz) continuum emission, with a total flux of 0.8 Jy. The astrometry was checked by using the Ganymede data to phase-calibrate the 1924-292 data, and mapping 1924-292. The map showed 1924-292 as a point source with a position error of 0.2 arcsec.

The 690 GHz band data were more difficult to process, in part because of instrumental problems. Three of the correlator’s 24 spectral bands were defective on some baselines. One receiver lost phase lock for 45 min during the track, and relocking the receiver produced a phase jump on the baselines to that antenna. All data taken with $T_{\text{sys}} > 6000$ K (on either antenna of any baseline) were discarded. Finally, much of the data were taken after sunrise, when the pointing of the array antennas is always degraded. The cross-correlation amplitude of Ganymede was checked on all baselines, and the source data were discarded whenever the nearest (in time) Ganymede scans had low amplitudes. Altogether, roughly 1/3 of the 690 GHz data were discarded for these reasons. Saturn, 3C 273, and Ganymede again were used to provide instrument bandpass calibration. 1924-292 was not detected on short timescales in the 690 GHz data, so only Ganymede could be used in the gain calibration. Ganymede was resolved by the array at 690 GHz, which caused the amplitude of this calibrator to pass through zero as the phase jumped by 180 degrees several times during the track. Projected baselines for the on-source data ranged from 17.9 to 230 kilolambda. The 450 micron (690 GHz) continuum emission from GoHam was detected with a total flux of 1.5 Jy, but $\text{CO } J=6-5$ line emission was not detected to a typical noise level in the maps of ~ 1 Jy/beam.

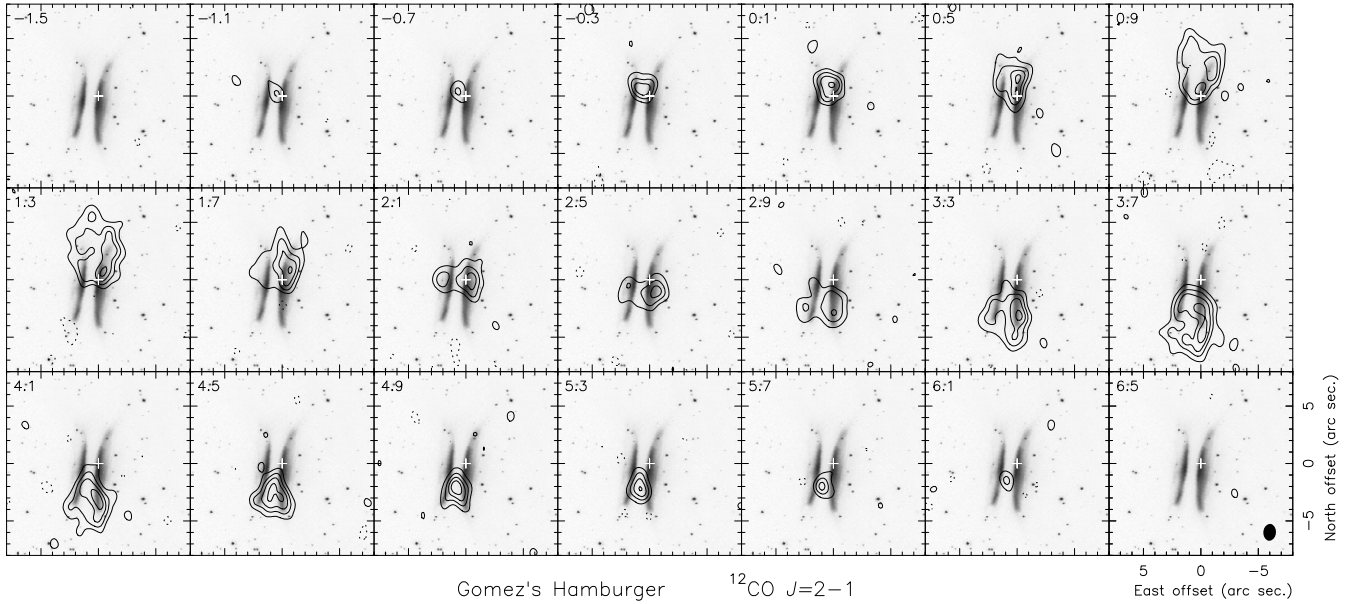


Fig. 1. Channel maps of the $^{12}\text{CO } J=2-1$ line from Gomez’s Hamburger, continuum has been subtracted. First contour and contour step are 0.28 Jy/beam, approximately equal to 3σ ; negative values are represented by dashed contours. The LSR velocity in km s^{-1} for the center of each channel is indicated in the upper left corner. The J2000 coordinates of the reference position, the cross in the maps, are RA = 18:09:13.37, Dec = -32:10:49.5. In the last panel, we represent the synthetic beam at half-intensity (black ellipse). The HST image is also shown for comparison. See details in Sect. 2.

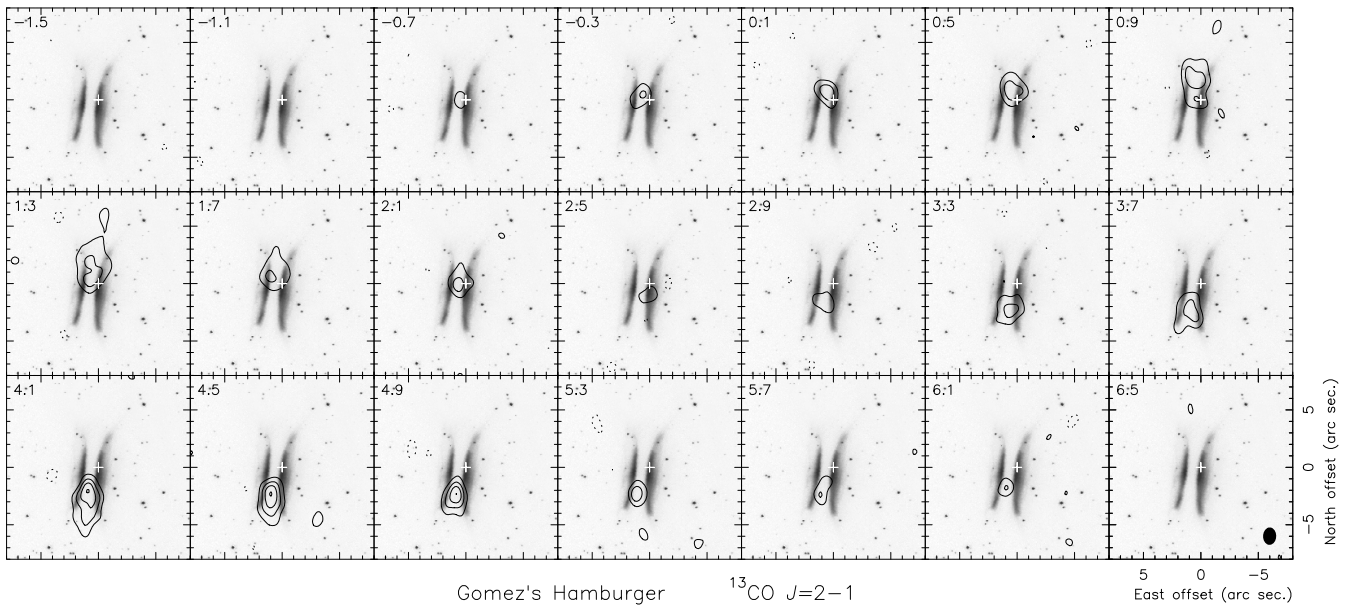


Fig. 2. Same as Fig. 1, but for the channel maps of the $^{13}\text{CO } J=2-1$ line observed from Gomez’s Hamburger. First contour and contour step are also 0.28 Jy/beam.

Mapping was completed with the NRAO AIPS package. The synthesized beam shapes were $3''.07 \times 1''.35$ with major axis position angle of $\text{PA} = 37.4^\circ$ for the $\text{C}^{17}\text{O } J=3-2$ maps, $2''.95 \times 1''.31$ with $\text{PA} = 37.6^\circ$ for the $^{12}\text{CO } J=3-2$ maps, and $3''.59 \times 0''.82$ with $\text{PA} = -5.7^\circ$ for the 450 micron continuum map. The resulting maps per velocity channel of the four detected lines are shown in Figs. 1–5.

In Figs. 1 and 2, we also show the HST image of GoHam, to allow a more robust comparison with the CO emission and between both ^{12}CO and $^{13}\text{CO } J=2-1$ lines. In Fig. 3, we show a zoom of the data from Figs. 1 and 2 for the emission at velocities 0.9 and 4.1 km s^{-1} LSR, expected to represent the emission

from regions closer to the plane of the sky. In displaying the HST images, we chose the beautiful color image from press release 2002-19 provided by the HST newscenter (obtained from WFPC2 images, filters: *F675W*, *F555W*, *F450W*), see <http://hubblesite.org/newscenter/>. The coordinates were derived from the NICMOS images in the HST archive (taken on April 12, 2006, HST project 10 603, P.I.: Padgett; NICMOS images were more directly comparable to the press release image than the archive WFPC2 data). We used the Aladin viewer and database. We recall that these images have not yet been published in the specialized literature and that a deep analysis of the HST imaging of GoHam is beyond the scope of this paper.

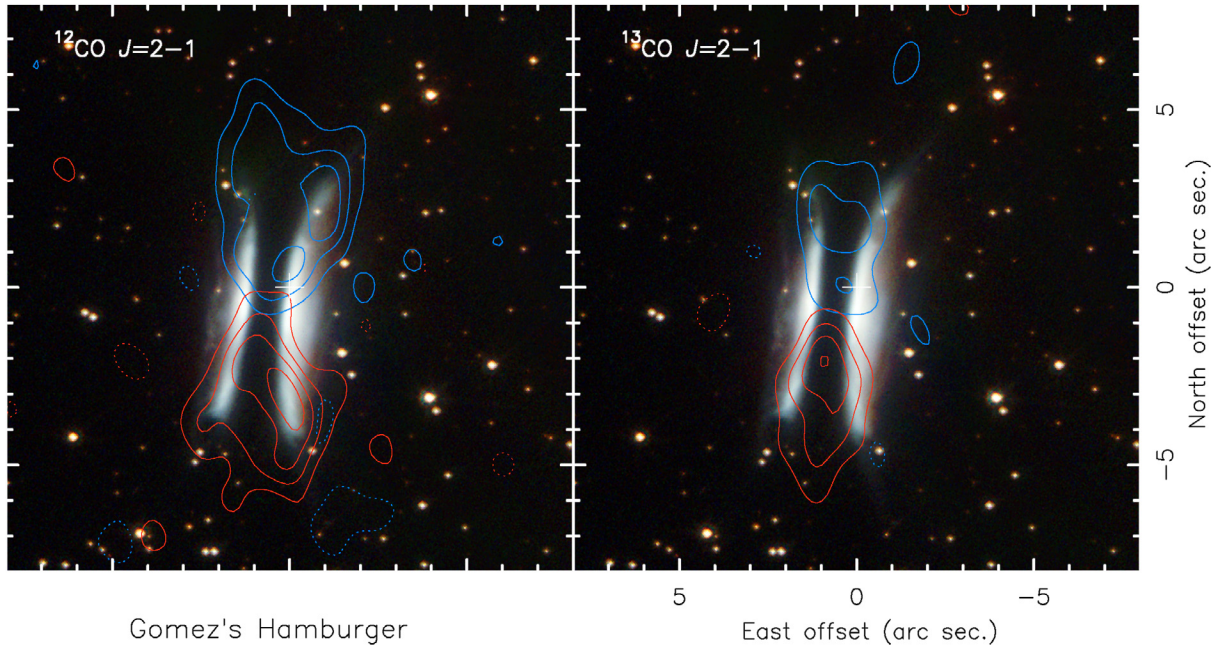


Fig. 3. Zoomed ^{12}CO and ^{13}CO $J=2-1$ emission for velocities 0.9 and 4.1 km s^{-1} , respectively blue (north) and red (south) contours, superposed to the HST image of GoHam; from Figs. 1 and 2, see further details in Sect. 2.

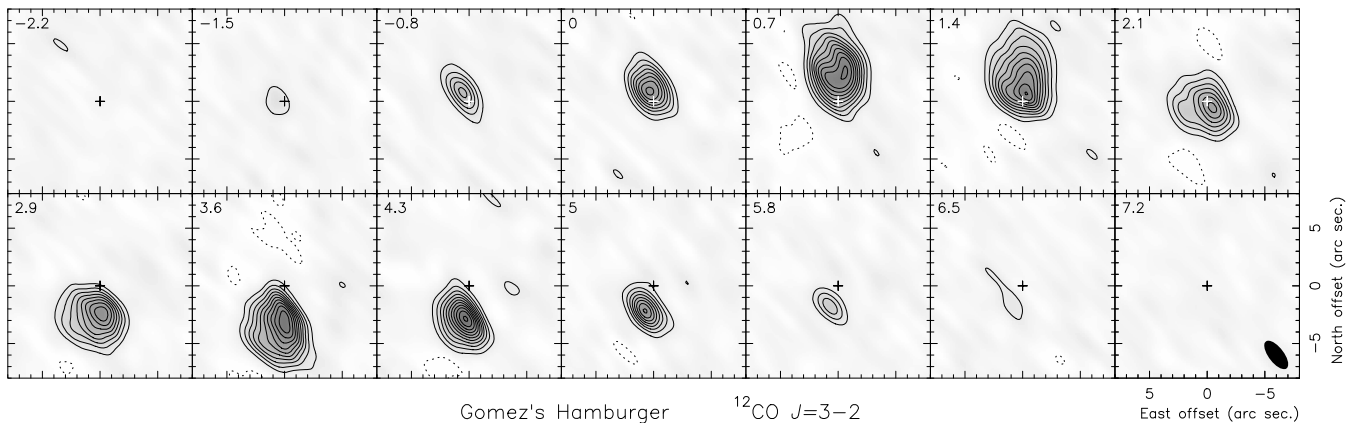


Fig. 4. Same as Fig. 1, but for the channel maps of the ^{12}CO $J=3-2$ line observed from Gomez's Hamburger. First contour and contour step are 0.5 Jy/beam . Note that the spectral and spatial resolutions of these observations are somewhat poorer.

3. CO emission model

To extract as much information as possible from our maps, we have used a code that simulates the emission from a rotating model disk. Our model provides brightness distributions for LSR velocity channels that are directly compared with the observations. We assume a shape of the CO cloud and a spatial distribution of the velocity, temperature, density, and CO relative abundance. Given these parameters, our code calculates the emissivity of the lines at each point in the disk, and then the brightness along a number of lines of sight by solving the full radiative transfer equation. Opacity effects and velocity shifts are accurately taken into account. This brightness distribution is then convolved with the synthetic beam, and images with the same units as those observed are produced.

The code itself is similar to that described by Bujarrabal et al. (2008), Paper I (see further details there, including discussions about the basic assumptions). The method used to find the best-fit solution and the uncertainties in the derived parameter values are presented in Sect. 3.4 and the Appendix.

However, the disk model used here is far more complex than that in Paper I, mainly because the large amount of empirical data presented now allows us to undertake an accurate description of the structure and physical conditions in the disk. We attempted to reproduce all our SMA maps from the model predictions and, at the same time, to keep our disk model as consistent as possible with theoretical ideas about the properties of rotating disks around young stars. As we will show in the next subsections, the model has become relatively complex, but the different disk components always correspond to features identifiable in our data.

3.1. Disk shape and dynamics

From a first inspection of both our maps and the HST image (Figs. 1–3), it is clear that the nebula is essentially a rotating disk seen almost edge on, showing significant axial symmetry and Keplerian dynamics. We can also see that the disk is roughly flaring, being significantly wider at larger distances from the center.

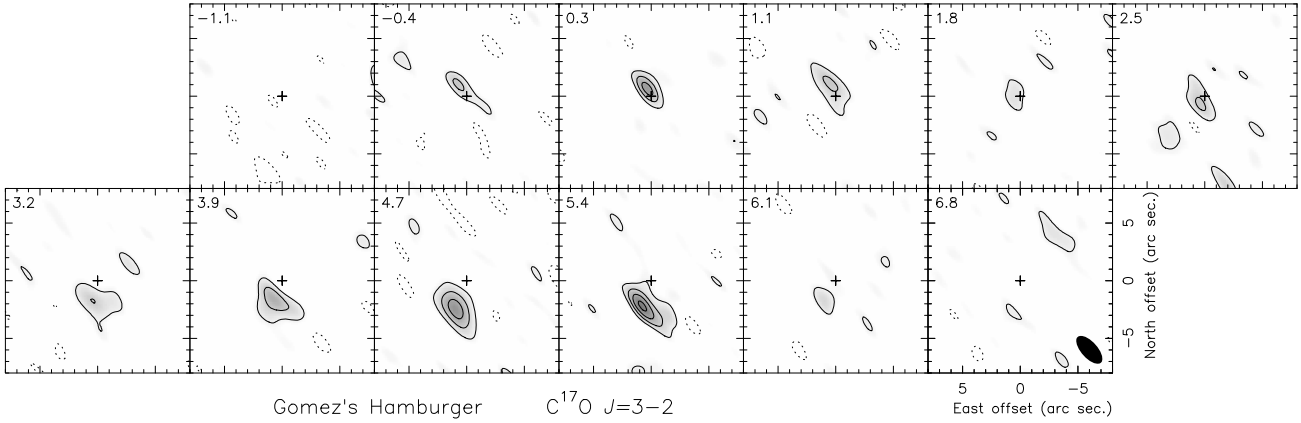


Fig. 5. Same as Fig. 3, but for the channel maps of the $C^{17}O$ $J=3-2$ line observed from Gomez’s Hamburger. First contour and contour step are 0.3 Jy/beam.

The disk symmetry axis is almost in the plane of the sky, and slightly tilted such that the western part of the disk points towards us. The projection of the disk symmetry axis on the sky plane is almost in the east-west direction with a position angle $PA \sim 85^\circ$, i.e., the disk appears almost parallel to the declination axis.

We assume accordingly that the emission originates in a flaring disk in Keplerian rotation and showing axial symmetry. Our calculations confirm that the observations can be explained by these assumptions. Two dimensions are then sufficient, i.e., r , the distance to the disk axis, and z , the distance to the disk equator.

We assume the simplest flaring geometry with a disk width that is proportional to r . In our case, the disk boundaries represent the region where CO is still abundant, before it is significantly photodissociated (due to the UV radiation from the central star or from the galactic background). We note, however, that the comparison of the ^{12}CO maps with the HST scattered light images (Figs. 1 to 3) suggests that the ^{12}CO disk occupies the entire nebula. To keep the model as simple as possible, we assume constant CO abundance, $X(CO)$, and isotopic ratios. We note that the CO abundances and density laws are not independent parameters in our model; therefore, the value of $X(^{12}CO)$ given here is an assumption chosen to be reasonably in agreement with expectations. We recall that the molecular abundances in the inner regions of the disk may be significantly smaller than the usual ones in the interstellar medium, mainly due to depletion onto grains (see discussion in, e.g., Panić et al. 2008; Thi et al. 2004, and references therein). As mentioned above, we expect significant dissociation of CO in the outer regions of the disk. We must therefore keep in mind that, although the CO abundance assumed here for ^{12}CO , i.e., 10^{-4} , is moderate, its value could be still lower in certain regions.

As we can see in our ^{12}CO $J=2-1$ maps, particularly at 1.3 km s^{-1} LSR, the shape of the outer part of the disk seems to be rounded, instead of flaring (at large distances, $r > R_m$, from the rotation axis). The model predictions differ clearly from the observations if we assume that the flaring geometry continues to the outer disk radius. The shape of the disk is accordingly given by the following parameters: the outer maximum and inner minimum disk radii, R_{out} and R_{in} ; the intermediate radius out to which the disk is flaring, R_m ; and the width at a given value of r , $H(r_0)$, such that $R_{in} \leq r_0 \leq R_m$. Between R_m and R_{out} , the disk width is assumed to vary according to an elliptical function. These assumptions are consistent with calculations of the CO

abundance variations in rotating disks, see, e.g., Jonkheid et al. (2006, 2007). See the resulting disk shape in Fig. 7.

The kinematics is assumed to be given by the rotational velocity, following a Keplerian law with r , i.e., varying proportionally to $1/\sqrt{r}$. As in Paper I, we find that some amount of local turbulent dispersion helps to reproduce the data, but that its value must be kept small. We then assume the existence of a constant local dispersion V_{turb} .

3.2. Density and temperature

Direct inspection of our data suggests that the density and temperature distribution must follow relatively complex laws, which we introduce in our model, trying to keep them consistent with general theoretical ideas.

First of all, we can see a remarkable difference between the ^{12}CO and ^{13}CO $J=2-1$ maps (see Figs. 1 and 2 and a zoom of intermediate velocities in Fig. 3). The ^{13}CO brightness distribution is significantly narrower (less extended in the direction of the disk axis, which is almost equivalent to the east-west direction) and shorter (less extended in the disk plane direction). Nevertheless, in regions in which both lines are intense (in the disk plane, slightly northwards and southwards from the star), the ^{12}CO $J=2-1$ brightness is only slightly higher. On the other hand, in the disk edges, where only ^{12}CO emission appears, the brightness of this line is often significantly higher than in the central regions (where both $J=2-1$ transitions are detected).

Since ^{13}CO emission is certainly expected to be much less optically thick than ^{12}CO emission and both lines are easily thermalized, this different behavior between them obviously means that there are wide outer edges of the disk in which the density significantly decreases and the temperature increases. These edges are both more or less parallel to the disk equator (appearing from certain values of $|z|$) and perpendicular to it (appearing from certain values of r). This behavior is particularly noticeable in the direction perpendicular to the plane, i.e., sharp variations in density and temperature occur from a certain distance to the disk equator, and are particularly well identified in the maps. We can also see in our ^{12}CO $J=2-1$ maps that one of these edges parallel to the equator (so, almost parallel to the north-south direction), the western one, is significantly more intense than the other. This is due to a simple radiative transfer effect: the emission from the eastern edge is absorbed by the cooler and opaque inner regions, which does not occur for the emission from the other side, which is closer to us. As we will see, our model

reproduces this phenomenon convincingly. Nothing comparable, of course, is seen in the optically thinner ^{13}CO emission, which, because of the low density of the hot edges, is only intense in the dense central regions.

Therefore, to reproduce the observations of the different lines, we must introduce several components in our density and temperature laws. At a minimum, we need a cool, dense region close to the equator, plus two edges of significantly lower density and higher temperature (which are more or less parallel to the equator and separated quite distinctly from the previous equatorial region), plus an outer region far from the disk axis with similar but smaller variations in these parameters.

We finally introduce a new correction: to explain the relatively intense emission for regions close to the central star, in spite of their small volume in a flaring disk, the density and temperature must increase from the standard values at small enough distances from the star. As we discuss in Appendix A.2, the physical properties of these regions, unresolved in our observations, are not well determined.

The equatorial density and temperature (n_{eq} , T_{eq}) are supposed to follow potential laws, $n_{\text{eq}}(r) \propto 1/r^{\alpha_n}$ and $T_{\text{eq}}(r) \propto 1/r^{\alpha_T}$. These laws are often found to be compatible with studies of molecular gas in disks around young stars (e.g., Dutrey et al. 2007), and we find that these simple laws are sufficient for modeling the amount of information contained in our data. In practice, we assume that α_n is not a free parameter but equal to 1, a value with which we can reproduce our results. We note that the assumption of a constant accretion rate, sometimes adopted when deriving the density law, can hardly be justified in a relatively evolved object such as GoHam, whose central star is barely accreting material.

The variation in the density with z , the distance to the equator, is assumed to be given by the vertical equation of hydrostatics (see e.g. Dullemond et al. 2007):

$$\frac{dP}{dz} = -\rho \Omega^2 z, \quad (1)$$

where the pressure is given by $P = kT/m_p$, m_p is the average weight of the gas particles, ρ is the density, and $\Omega(r)$ is the angular velocity.

For a constant temperature with z , $T(r, z) = T_{\text{eq}}(r)$, $n(r, z)$ is given by:

$$n(r, z) = n_{\text{eq}}(r) e^{-\frac{z^2 C_1}{2T_{\text{eq}}(r)}}, \quad (2)$$

where $C_1 = \Omega^2(r) m_p/k$ is a function of r , not of z .

To include the dramatic change in temperature and density from a value of $|z|$, we assume that, when $n(r, z)$ reaches a certain fraction of $n_{\text{eq}}(r)$, the temperature changes by a factor, F_T . The value of F_T is obtained by comparing the observations with the model predictions (see Table 1 and Sect. 4), as well as the fraction of the density at which the jump must appear (1/10 was found to yield acceptable model results).

We assume that there is also a jump in the density at this point, by a factor F_n , where F_n can be calculated from the equation of hydrostatics, written in the form:

$$\frac{1}{\rho} \frac{dP}{dz} = -\frac{z C_1}{T} - \frac{1}{T} \frac{dT}{dz}. \quad (3)$$

For a very steep discontinuity in T :

$$\frac{1}{\rho} \frac{dP}{dz} \sim -\frac{1}{T} \frac{dT}{dz}, \quad (4)$$

whose solution, for a jump between T_0 and T_1 , is:

$$\frac{\rho_1}{\rho_0} \sim \frac{T_0}{T_1}. \quad (5)$$

So, if the temperature varies at a given value of z , z_j , by a factor F_T , the density must vary at the same point by a factor $F_n = 1/F_T$. Beyond this point, for $z > z_j$, we assume that the temperature remains constant, and the density follows the law already inferred for constant temperature:

$$n(r, z) = n(r, z_j) e^{-\frac{C_1}{2T(r, z_j)}(z - z_j)^2}, \quad (6)$$

where $z > z_j$ and $n(r, z_j)$ and $T(r, z_j)$ denote the density and temperature just beyond the jump at z_j .

For the law that we assume for $n_{\text{eq}}(r)$ (i.e., $n_{\text{eq}}(r) \propto 1/r$), the condition for the discontinuity we are imposing, i.e. that $n(r, z)/n_{\text{eq}}(r)$ is smaller than a certain constant factor, is roughly equivalent to assuming that the jump appears for a fringe roughly parallel to the outer limit to the CO-rich disk in z . This is reasonable, since both the photodissociation of CO and the gas overheating are expected to be physically caused by the outer radiation field.

We have mentioned that T and n must also depart from our standard law in the outer disk, for $R_m < r < R_{\text{out}}$; again, n must show a decrease and T must increase to explain the ^{12}CO and $^{13}\text{CO } J=2-1$ emission from regions far from the symmetry axis. In this case, the n and T variations are assumed to be unrelated. See the finally adopted laws in Table 1 and Fig. 7. We note that the required change in T is small, but n must strongly decrease to explain the lack of ^{13}CO emission (and the decrease in the $^{12}\text{CO } J=2-1$ intensity close to R_{out}). In any case, the accuracy of the density value determined at the largest distances from the axis is poor, since it depends mostly on the intensity of only one line, which is (moderately) optically thick (see Appendixes). We note that, for the adopted physical conditions, the density in regions where r is slightly larger than R_m is high enough to allow detectable emission of ^{13}CO and $^{12}\text{CO } J=2-1$ for some LSR velocities. The central velocities of our $^{12}\text{CO } J=2-1$ maps show emission even from the outermost parts of the disk.

3.3. Other parameters

The inclination of the rotation axis with respect to the plane of the sky must be low, as implied by the optical and CO images. The projection of this axis on the plane of the sky is obviously at a position angle, PA, that is slightly smaller than 90° . We note that both parameters may in fact vary with r , since this large disk may be warped at some degree. This appears to be the case if we compare the inclinations in the CO maps for $V_{\text{LSR}} \sim 1.3-1.7 \text{ km s}^{-1}$ and for 0.9 or 3.3 km s^{-1} . It is probable that some regions of the disk rotate around an axis (in projection) at PA $\sim 80^\circ$, while other regions rotate around PA $\sim 90^\circ$.

The distance was discussed in Paper I and Sect. 1, where the uncertainties in its value were emphasized. We adopt a distance of 300 pc.

The systemic velocity is quite well determined from our maps of CO lines, to an accuracy higher than 10%. The given value in Table 1 is compatible with all observations presented here.

3.4. Fitting procedure and results

We chose the most suitable set of parameters by directly comparing the observed and synthetic images. We propose that

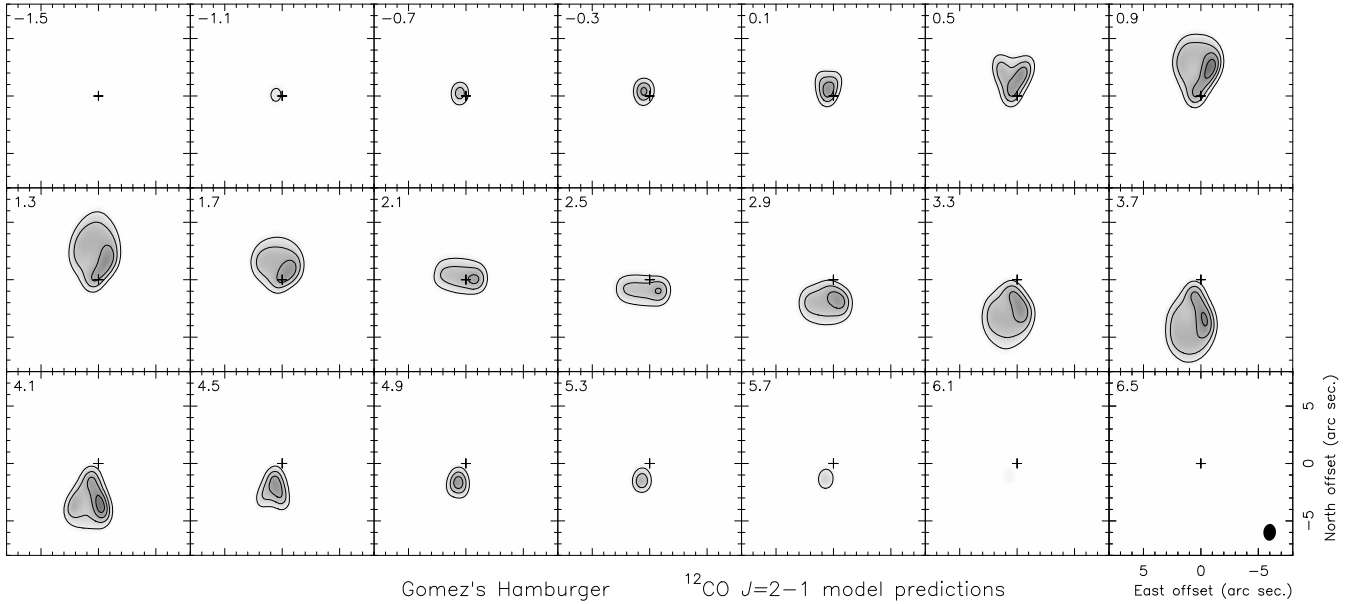


Fig. 6. Predictions of the $^{12}\text{CO } J=2-1$ line brightness from our best-fit model for the GoHam disk. The spatial scale and contours are the same as in the observations, Fig. 1.

the comparison in the sky plane, and not in the transformed uv plane, is possible in our case because of the relatively large extent of the source. On the other hand, the large number of parameters, required to describe the various components implied by the observational features, and the different significance of them, prevent any systematic, blind fitting. (See detailed discussion in Appendix A.1.) The ^{12}CO and $^{13}\text{CO } J=2-1$ images, which contain much information, provided the basic data for this comparison.

In Appendix A.1, we also present in detail the criteria followed to choose the acceptable models. The residual images, i.e., the difference between the observed and theoretical images, must have an rms noise in regions where the emission appears smaller than ~ 1.5 times that found in nearby regions (that includes only the noise of the observations). The residual images must also exhibit contours smaller than ~ 3 times the noise level or ~ 2 times systematically. For instance, for a model to be acceptable, we must not find in the resulting $^{12}\text{CO } J=2-1$ residuals two positive or negative contours; we note that the observed $^{12}\text{CO } J=2-1$ image does show one contour features that are due to the observational noise. For an acceptable model, the regions in the residual images in which emission was present appear, therefore, to differ only slightly from those in which there was no emission.

In Appendix A.2, we discuss the uncertainty in the main parameters of the model, given by the values of each parameter that, while the others remain unchanged, lead to results that clearly do not satisfy these conditions.

The conditions for the model predictions to be acceptable are relaxed for the relatively strong emission detected at about $4.5\text{--}5.5 \text{ km s}^{-1}$, which has no counterpart in the equivalent blue-shifted emission. We propose that this emission excess is due to a condensation in the rotating gas (Sect. 4 and Appendix A.3). Our model assumes axial symmetry and cannot reproduce this emission excess; we preferred to fit mostly the emission in the other velocities and to discuss separately this intense clump (Sect. 4.1).

We present in Fig. 6 and in the Appendixes some examples of the resulting model maps and residuals. Table 1 and Fig. 7 present the values of the fitted parameters.

4. Results and conclusions

Our SMA observations of $^{12}\text{CO } J=2-1$, $^{13}\text{CO } J=2-1$, $^{12}\text{CO } J=3-2$, and $\text{C}^{17}\text{O } J=3-2$ in Gomez’s Hamburger (Sect. 2, Figs. 1 to 5) yielded high-quality maps. The maps were satisfactorily reproduced by our model of disk in Keplerian rotation (see Sect. 3, Fig. 6, and Appendix). From these maps and our model fitting of the data (see Sect. 3), we derived the main structure, dynamics, and physical conditions of the nebula (see parameters of the model and best-fit results in Sect. 3, Fig. 7, and Table 1). We assume a distance of 300 pc, see discussion in Bujarrabal et al. (2008, Paper I) and Sect. 1; the dependence of the fitting on the distance is given in Table 1. Further discussion on the fitting procedures and accuracy are given in the Appendixes.

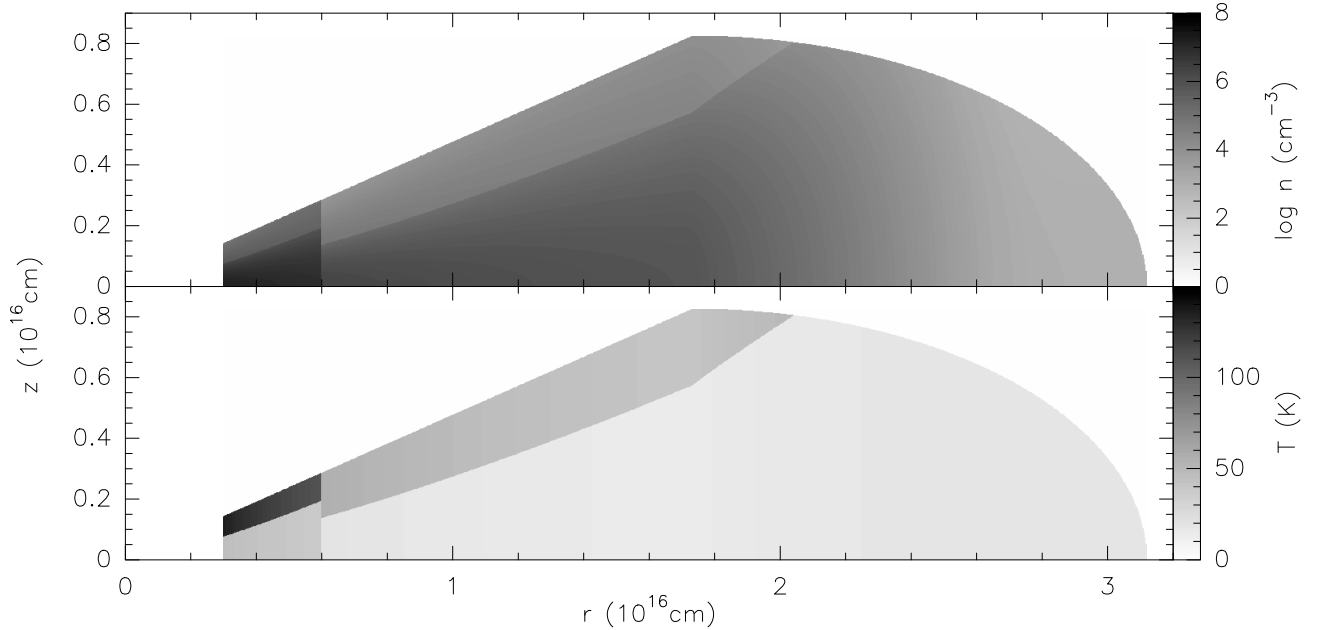
The CO emitting gas in GoHam forms a rotating disk that is probably coincident with the entire nebula, since the CO extent is even larger than the HST image (showing scattered light and absorption by dust grains, see Figs. 1–3). We recall, however, that the disk shape given here is that of the region in which CO is rich. Other nebula components in which molecules are severely underabundant, due to photodissociation by the interstellar or stellar UV field or to depletion onto grains, are not probed by our maps.

Our data confirm the previous conclusion (Paper I) that the disk is almost exactly in Keplerian rotation and has a clear axial symmetry. However, we infer, mainly from the $^{13}\text{CO } J=2-1$ maps (Figs. 2, 3) and their comparison with the model predictions, that there is a condensation in the southern disk that has no counterpart in other regions of the nebula (see discussion on its properties and meaning in Sect. 4.1).

The general dynamics and structure of the nebula are relatively well determined from the maps. We note that the shape of the model disk corresponds to the region in which, due to shielding from the external UV field, CO is still abundant.

Table 1. Structure and physical conditions in the molecular disk of Gomez’s Hamburger, derived from our model fitting of several CO rotational lines. Dependence on the assumed distance is given in the relevant cases. Other parameters of the modeling are also given.

Parameter	Law	Values	Comments
Outer radius		$R_{\text{out}} = 3.1 \times 10^{16} \left(\frac{D(\text{pc})}{300}\right) \text{ cm}$	
Intermediate radius		$R_{\text{in}} = 1.7 \times 10^{16} \left(\frac{D(\text{pc})}{300}\right) \text{ cm}$	
Inner radius		$R_{\text{in}} = 3 \times 10^{15} \left(\frac{D(\text{pc})}{300}\right) \text{ cm}$	
Disk thickness	linear	$H(10^{16} \text{ cm}) = 9.5 \times 10^{15} \text{ cm}$	
Tangential velocity	$V_t \propto 1/\sqrt{r}$ (Keplerian)	$V_t(10^{16} \frac{D(\text{pc})}{300} \text{ cm}) = 2.1 \text{ km s}^{-1}$ central mass: $3 \left(\frac{D(\text{pc})}{300}\right) M_{\odot}$	
Temperature (equator)	$T_{\text{eq}} \propto 1/r^{\alpha_T}$	$T_{\text{eq}}(10^{16} \frac{D(\text{pc})}{300} \text{ cm}) = 16 \text{ K}$ $\alpha_T = 0.3$	+ increase in the edges, by a factor 3 + increase beyond R_{in} , $T(R_{\text{out}}) = 17 \text{ K}$ + increase within $2 \times R_{\text{in}}$, by a factor of 2
see text and Fig. 7			
Gas density (equator)	$n_{\text{eq}} \propto 1/r^{\alpha_n}$	$n_{\text{eq}}(10^{16} \frac{D(\text{pc})}{300} \text{ cm}) = 1.5 \times 10^6 \left(\frac{300}{D(\text{pc})}\right) \text{ cm}^{-3}$ $\alpha_n = 1$	+ decrease with z , following hydrost. eq. + decrease beyond R_{in} , $n_{\text{eq}}(R_{\text{out}}) = 10^3 \text{ cm}^{-3}$ + increase within $2 \times R_{\text{in}}$, by a factor of 2
see text and Fig. 7			
Relative abundances	constant	$X(^{12}\text{CO}):X(^{13}\text{CO}):X(\text{C}^{17}\text{O}) = 10^{-4}:1.5 \times 10^{-6}:2 \times 10^{-7}$	assumed value for $X(^{12}\text{CO})$
Other parameters		Values	Comments
Axis inclination from the plane of the sky		6°	from optical and CO data
Axis inclination in the plane of the sky (PA)		85°	from optical and CO data
Distance		300 pc	from luminosity and mass values (Sect. 1)
LSR systemic velocity		2.5 km s^{-1}	from CO data

**Fig. 7.** Density and temperature distributions in our best-fit model. r is the distance from the rotation axis, and z is the distance to the equator.

The shape that we deduce is compatible with the general structure expected for the CO-rich parts of disks around young stars, see, e.g., [Jonkheid et al. \(2006, 2007\)](#).

The model distributions of the number density (n) and temperature (T) require deeper discussion. The difference between the distributions of ^{12}CO and ^{13}CO $J=2-1$ emission is particularly useful for this purpose. The bright rims, more or less parallel to the equator, clearly seen in the optically thick ^{12}CO emission are not present in ^{13}CO . Since ^{13}CO $J=2-1$ is certainly much less opaque than ^{12}CO $J=2-1$, this indicates a significant increase in temperature and decrease in density in regions sufficiently separated from the equator. We note that this decrease in

density with distance from the equator, z , appears in our model as a result of the jump in temperature, since the variation in density with z is assumed to be given by the equation of hydrostatics for a rotating disk. Our model reproduces the observations by assuming a characteristic (sharp) increase in temperature by a factor of 3. We note that the ^{13}CO $J=2-1$ emission originates only in the opaque equatorial disk seen in the HST images (Figs. 2 and 3), while the bright rims detected in ^{12}CO $J=2-1$ at large distances from the equator correspond to the flaring-disk edge that appears in the visible and NIR as a result of the scattering of stellar light by dust (Figs. 1 and 3).

Similar changes in the physical conditions within the disk were predicted from theoretical considerations (see e.g. Dullemond et al. 2007). Some previous maps of disks around young stars also exhibited an increase in temperature of this order (e.g., Dartois et al. 2003).

A comparison of the ^{12}CO and ^{13}CO maps also infers that n decreases and T increases at large distances from the rotation axis (large values of r , even on the equator), because of the significantly less extended emission of $^{13}\text{CO } J=2-1$ and the relative maxima found in $^{12}\text{CO } J=2-1$ at such large distances. In this case, the variations in temperature and density are assumed to be independent, and we indeed find that the factor of density decrease must be higher. A general description of the spatial distribution of the physical conditions can be seen in Fig. 7. We recall that we assume that the molecular abundances are constant within the entire disk, because existing data do not allow us to consider independently variations in the abundances and variations in the density and temperature. Therefore, the decrease in density at large r could (at least partially) reflect a decrease in the ^{13}CO abundance in those regions. (This does not affect the remaining conclusions: the temperature must increase at high values of both z and r , to explain the higher ^{12}CO intensity, and the density for high z must decrease to satisfy the hydrostatics equations.)

A clear asymmetry is visible in the ^{12}CO brightness distribution with respect to the disk equator, i.e., between the eastern and western parts of the nebula (Fig. 1). This effect is due to self absorption: the cold equator absorbs the emission originating in the hot, outer regions at high z that are placed behind it (corresponding to the east part of the CO image), which of course does not affect the emission of the hot layer that is closer to us. This asymmetry is reproduced well by our model calculations, which accurately take into account opacity effects and radiative interactions between the different parts of the nebula.

We note the low degree of local turbulence inferred from the model fitting, $\lesssim 0.1 \text{ km s}^{-1}$. Small values of the microturbulence velocity are often found in rotating disks (e.g., Panić et al. 2008), even in the rare cases of disks rotating around evolved stars (Bujarrabal et al. 2005).

The total central mass responsible for the observed rotation is deduced to be $\sim 3 M_{\odot}$. We have seen in Sect. 1 and Paper I that this mass seems high compared to that derived by comparing the total luminosity with evolutionary tracks, $\sim 2 M_{\odot}$ (with high uncertainties). As discussed in Paper I and Sect. 1, the mass value deduced from the observed rotation may include as much as $\sim 0.5 M_{\odot}$ as a contribution of the dense, very inner regions of the disk (which are not well probed by our observations, because of their insufficient resolution). Therefore, the comparison of the mass values derived from evolutionary tracks and disk dynamics may still imply the presence of a binary star in GoHam. The conclusion about the binary nature of the central star depends, unfortunately, on the comparison between theoretical evolutionary tracks and the uncertain values of the stellar luminosity and surface temperature, which cannot at present be determined with sufficiently high accuracy (see Paper I and Sect. 1).

Our model also estimates the total mass of the (extended) disk. By integrating the model density, we derive a value of $\sim 0.01 M_{\odot}$. As in our previous work (Paper I), we determine a disk mass value that is far smaller than the total mass derived from dust emission ($\sim 0.3 M_{\odot}$; Sects. 1, 3). This may be due to a strong gas depletion onto grains, mainly in the densest regions of the disk (Dutrey et al. 1997; Thi et al. 2004; Panić et al. 2008), which could yield a higher dust mass and lower molecular abundances than expected. We propose that this effect could

explain at least in part the discrepancy between the mass derived from dust emission and from CO maps. Unfortunately, the dust continuum emission was found to originate predominantly in the very center of the disk, which is poorly mapped by our $1''$ -resolution CO line maps, avoiding a proper comparison of both distributions. A future study of the effects of depletion on the mass determinations in this source will require significantly deeper maps of the continuum emission, tracing dust to distances comparable to those observed in CO emission, as well as higher resolution maps of CO lines, accurately mapping the inner disk regions.

4.1. The southern condensation

As discussed in Sect. 3, we detect an asymmetry in our data, particularly in the $^{13}\text{CO } J=2-1$ maps, that cannot be accounted for by an axially symmetric model (Figs. 2, 3). We observe an emission excess in the southern part of the nebula, at about $1'3$ from the nebula center ($6 \times 10^{15} \text{ cm}$ for the assumed distance of GoHam) and between about $+4.5$ and $+5.5 \text{ km s}^{-1}$ LSR, which has no counterpart in the corresponding northern emission at more negative velocities. This asymmetry cannot be due to opacity or excitation effects, because it is clearly more conspicuous in the $^{13}\text{CO } J=2-1$ and $\text{C}^{17}\text{O } J=3-2$ lines than in the $^{12}\text{CO } J=2-1$ one, which is more opaque, and the $^{12}\text{CO } J=3-2$ line, which requires a higher excitation. Since the intense maximum is more evident in $^{13}\text{CO } J=2-1$, which is mostly optically thin, we propose that this is caused by a condensation, i.e., a significant increase of the density in those regions. We discuss in this section the properties and possible origin of this condensation, which could be protoplanetary.

It is remarkable that such strong asymmetries between regions with relatively positive and negative velocity are not frequent in CO-rich rotating disks (Dutrey et al. 2003; Piétu et al. 2005; Simon et al. 2000), even in observations of ^{13}CO lines. An exception may be the C^{18}O maps in DM Tau by Dartois et al. (2003, but not their ^{13}CO data), which exhibit an emission excess at certain velocities comparable to that in our ^{13}CO maps. More subtle departures from the Keplerian dynamics were also identified in AB Aur (as well as in our maps of GoHam; see discussion below).

We attempted to estimate the amount of mass represented by this excess brightness, although this observational feature is difficult to model because of the considerable lack of information about its nature. A lower limit can be obtained if we assume that the excess mass is proportional to the total additional intensity in $^{13}\text{CO } J=2-1$. The increase in line intensity at these velocities represents somewhat less than 20% of the total (velocity integrated) line intensity. Since the total mass inferred by our disk model is $\sim 0.01 M_{\odot}$, we deduce that the mass of the condensation is $\sim 1.5 \times 10^{-3} M_{\odot}$, almost identical to the mass of our planetary system or to the mass of Jupiter.

We recall that this mass value must be considered as a lower limit. The excess mass is proportional to the total extra intensity in $^{13}\text{CO } J=2-1$ if this line is completely optically thin and the excitation in the clump is the same as in the surrounding gas. We know that the first assumption is not completely true even for lines of sight that do not intersect the condensation. The second assumption is also improbable, since the density increase must be important; moreover, we note that the opaque $^{12}\text{CO } J=2-1$ line also exhibits some intensity increase in these regions, suggesting that they are hotter than nearby regions. The presence of some opacity also in $^{13}\text{CO } J=2-1$ will lead to a perhaps significant mass underestimate in our simple estimate. The effects

of the different excitation should be less important. A higher excitation increases the partition function of the molecule and decreases the level population difference, which leads to lower emission in optically thin lines (although, of course, a higher temperature means a higher intensity when the optical depth is high). Therefore, both assumptions will in general lead to underestimates of the clump mass.

We performed a more robust estimate introducing a density increase in some parts of our model disk (destroying the axial symmetry). We estimate, first, that to model the asymmetry in the $^{12}\text{CO } J=2-1$ maps we need an excess temperature by a factor 1.5 in a southern disk region closer than 10^{16} cm. We then attempted to reproduce the $^{13}\text{CO } J=2-1$ data approximately by increasing the density by some factor, with respect to standard law (derived from fitting our entire data set, Sect. 3, Table 1). A significant factor (~ 10) is found to be necessary to account for the beam dilution and some incipient optical depth in this line. The model predictions for the southern brightness increase in $\text{C}^{17}\text{O } J=3-2$ are also consistent with the observations. See a detailed discussion on our tentative modeling of this clump in Sect. A.3. With these conditions, we find that the condensation contains a total mass $\sim 6 \times 10^{-3} M_{\odot}$, a few times the mass of our planetary system.

We note that these estimates do not exclude the presence of more compact components that are undetectable with our angular resolution. We also note that a proto-solar-system must contain a significantly higher mass than the final planetary system, since significant gas ejection is expected before planets form in these condensations. Finally, we recall our poor knowledge of the physical properties of these clumps and the poor observational information on it, which remains practically unresolved in our data, preventing any detailed modeling.

On the other hand, our fitting of the ^{13}CO emission at these velocities is only accurate for the clump intensity. In the observations, the brightness maximum appears to be displaced outwards by 0.5 arcsecond, with respect to the position expected from our fitting (see Appendix A.3). This effect cannot be avoided if we assume that the condensation is farther from the star, since the velocity field we assume (the same Keplerian law deduced from the fitting of the overall dynamics, Sect. 3) would then imply that its emission occurs at too low relative velocities. This displacement can easily be seen in the observations: we note the anomalously large distance from the star of the maximum in $^{13}\text{CO } J=2-1$ emission at about 5 km s^{-1} , compared to the brightness distributions at about 3.5 km s^{-1} . Therefore, the presence of a disturbance in the dynamics is necessary to explain the observed properties of the southern condensation, leading us to conclude that both the disturbance in the dynamics and the presence of a condensation are probably associated.

The standard conditions theoretically required to produce gravitational instabilities in the disk (e.g., Durisen et al. 2007) are not satisfied for this condensation. In GoHam, instabilities would only occur at a less than $\sim 10^{15}$ cm from the star, the distances on which detailed theoretical models tend indeed to predict the presence of protoplanets. The size inferred from our data for the condensation is also too large compared to the Hill sphere, which defines the gravitational domain of a protoplanet (e.g., Lissauer & Stevenson 2007), if we do not assume the presence of undetected compact components. In fact, the mass of the central component required by the large extent of the condensation would be $\sim 0.5-1 M_{\odot}$, i.e., that of a low-mass protostar.

From the observational point of view, however, other evidence of important condensations has been found at similar large distances from the star, probably due to disk instabilities. For

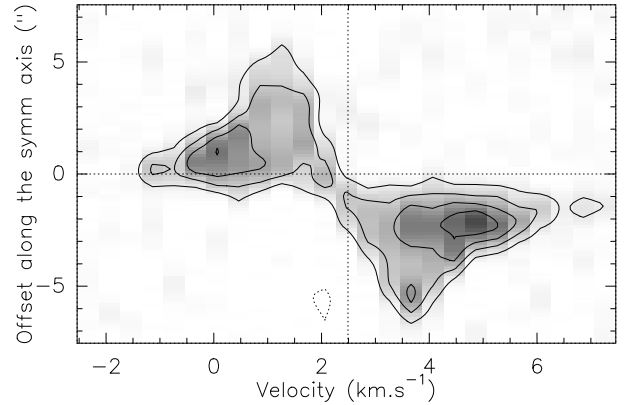


Fig. 8. Position-velocity diagram of the $^{13}\text{CO } J=2-1$ emission from GoHam, obtained along the disk direction ($\text{PA} = -5^\circ$). The southern emission excess can be seen at positive velocities.

instance, the well known spiral structure in AB Aur appears to be at a distance smaller than about 100 AU or 1.5×10^{15} cm (Oppenheimer et al. 2008; Millan-Gabet et al. 2006), but spiral-like dust condensations are also detected at several hundred AU (Fukagawa et al. 2004) and seem to have some counterpart in CO emission (Piétu et al. 2005; Lin et al. 2006). Piétu et al. (2005) and Lin et al. (2006) also detected departures from the general Keplerian velocity field in the spiral arms of AB Aur, comparable in magnitude to those found by us in GoHam. To compare our observations with previous results more effectively, we represent in Fig. 8 the position-velocity diagram along the disk direction in GoHam, obtained from our $^{13}\text{CO } J=2-1$ data, in which the excess emission is clearly seen at positive velocities. The p-v diagram in GoHam is found to be similar to that obtained by Lin et al. (2006) in AB Aur, in spite of the different angular and velocity scales. The deformation of the dynamics in AB Aur associated with the spiral instability therefore produces a velocity pattern similar to that found in Gomez’s Hamburger. On the other hand, Lafrenière et al. (2008) reported the detection, from direct imaging and spectroscopy, of a planet with a mass about 8 times higher than that of Jupiter at 5×10^{15} cm from a young star, although systems on such large scales appear to be rare (Lafrenière et al. 2007). Planets with a few times the mass of Jupiter have been also found around the A-type stars Fomalhaut and HR 8799 (Kalas et al. 2008; Marois et al. 2008), at quite large distances from the star, ~ 100 AU, although smaller than that of our condensation. Finally, we note the detection, from dust emission mapping at $\lambda = 1.3$ cm, of a condensation containing 14 times the mass of Jupiter at 65 AU from HL Tau, which was interpreted to be protoplanetary (Greaves et al. 2008).

The southern condensation could also be associated with the presence of a low-mass stellar or quasi-stellar companion, which is able to capture gravitationally a sizeable fraction of the overall disk material and may explain the anomalous dynamics found in the condensation. The contribution of the companion mass ($\lesssim 1 M_{\odot}$) to the total central mass could be necessary to explain that the mass value derived from the overall disk rotation (i.e., derived from data of extended regions and regardless of the peculiar kinematics of the condensation) is perhaps too high for the observed total luminosity; see above for more details.

In summary, we have identified a condensation in the southern part of the disk, about $1''3$ from the disk center, that probably contains a mass of a few times that of Jupiter. This

condensation could be protoplanetary, in a preliminary evolutionary stage. We have noted that theory predicts in general that planets tend to form at much smaller distances from the central star, although observational results support the formation of condensations at such long distances. This clump could also be due to material gravitationally captured by a stellar or quasi-stellar companion, whose presence has been proposed independently to explain the total central mass derived from the disk rotation velocity. We recall that the condensation seems to be associated with a significant local distortion of the general Keplerian velocity field of the nebula; this distortion could be explained if both the clump formation is due to the presence of a low-mass stellar companion or to gravitational instabilities within the disk.

Acknowledgements. We are grateful to Asunción Fuente and Mario Tafalla for very helpful comments on the manuscript.

Note added in proof. After this work was accepted, two papers appeared, predicting theoretically the formation of planets beyond 100 AU and discussing the conditions under which this may occur: Boley, A. C., 2009, *ApJ*, 695, L53; Veras, D., Crepp, J. R., & Ford, E. B., 2009, *ApJ*, 696, 1600.

References

- Berné, O., Joblin, C., Fuente, A., & Ménard, F. 2009, *A&A*, 495, 827
 Bujarrabal, V., Castro-Carrizo, A., Alcolea, J., & Neri, R. 2005, *A&A*, 441, 1031
 Bujarrabal, V., Young, K., & Fong, D. 2008, *A&A*, 483, 839 (Paper I)
 Dartois, E., Dutrey, A., & Guilloteau, S. 2003, *A&A*, 399, 773
 Dullemond, C. P., Hollenbach, D., Kamp, I., & D'Alessio, P. 2007, in *Protostars and Planets V*, ed. B. Reipurth, D. Jewitt, & K. Keil, 555
 Durisen, R. H., Boss, A. P., Mayer, L., et al. 2007, in *Protostars and Planets V*, ed. B. Reipurth, D. Jewitt, & K. Keil, 607
 Dutrey, A., Guilloteau, S., & Guelin, M. 1997, *A&A*, 317, L55
 Dutrey, A., Guilloteau, S., & Simon, M. 2003, *A&A*, 402, 1003
 Dutrey, A., Guilloteau, S., & Ho, P. 2007, in *Protostars and Planets V*, ed. B. Reipurth, D. Jewitt, & K. Keil, 495
 Fuente, A., Alonso-Albi, T., Bachiller, R., et al. 2006, *ApJ*, 649, L119
 Fukagawa, M., Hayashi, M., Tamura, M., et al. 2004, *ApJ*, 605, L53
 Greaves, J. S., Richards, A. M. S., Rice, W. K. M., & Muxlow, T. W. B. 2008, *MNRAS*, 391, L74
 Jonkheid, B., Kamp, I., Augereau, J.-C., & van Dishoeck, E. F. 2006, *A&A*, 453, 163
 Jonkheid, B., Dullemond, C. P., Hogerheijde, M. R., & van Dishoeck, E. F. 2007, *A&A*, 463, 203
 Kalas, P., Graham, J. R., Chiang, E., et al. 2008, *Science*, 322, 1345
 Lafrenière, D., Doyon, R., Marois, C., et al. 2007, *ApJ*, 670, 1367
 Lafrenière, D., Jayawardhana, R., & van Kerkwijk, M. H. 2008, *ApJ*, 689, L153
 Lin, S.-Y., Ohashi, N., Lim, J., et al. 2006, *ApJ*, 645, 1297
 Lissauer, J. J., & Stevenson, D. J. 2007, in *Protostars and Planets V*, ed. B. Reipurth, D. Jewitt, & K. Keil, 591
 Mannings, V., & Sargent, A. I. 1997, *ApJ*, 490, 792
 Mannings, V., & Sargent, A. I. 2000, *ApJ*, 529, 391
 Marois, C., Macintosh, B., Barman, T., et al. 2008, *Science*, 322, 1348
 Millan-Gabet, R., Monnier, J. D., Berger, J.-P., et al. 2006, *ApJ*, 645, L77
 Oppenheimer, B. R., Brenner, D., Hinkley, S., et al. 2008, *ApJ*, 679, 1574
 Panić, O., Hogerheijde, M. R., Wilner, D., & Qi, C. 2008, *ArXiv e-prints*, 806
 Piétu, V., Guilloteau, S., & Dutrey, A. 2005, *A&A*, 443, 945
 Ruiz, M. T., Blanco, V., Maza, J., et al. 1987, *ApJ*, 316, L21
 Simon, M., Dutrey, A., & Guilloteau, S. 2000, *ApJ*, 545, 1034
 Thi, W.-F., van Zadelhoff, G.-J., & van Dishoeck, E. F. 2004, *A&A*, 425, 955
 van den Ancker, M. E., de Winter, D., & Tjin A Djie, H. R. E. 1998, *A&A*, 330, 145
 Wood, K., Whitney, B. A., Robitaille, T., & Draine, B. T. 2008, *ApJ*, 688, 1118

Appendix A: Selection of the best-fit and the accuracy of the parameter values

A.1. Criteria for acceptable models

The general criterion we chose to select acceptable models was the comparison of the predicted images with the observed ones. Some authors (e.g., Dutrey et al. 2007; Pety et al. 2006; Isella et al. 2007) perform such a comparison in the Fourier transformed plane of the visibilities. The selected model parameters are then those yielding the smallest residuals, after considering ‘blind’ variations of the parameter values. Their method has the advantage of being objective and that uncertainties introduced by the cleaning process are avoided. Other authors (Mannings & Sargent 1997, 2000; Fuente et al. 2006) follow, however, a more intuitive approach, comparing directly the images.

In our case, the high number of free parameters prevents a blind analysis of the resulting residuals for any combination of parameter values, which would imply an exceedingly high amount of calculations. Even the definition of “free parameter” in this complex structure is difficult, and it is unclear at what extent we can vary all the disk properties. Even if theoretical constraints on our model parameters are taken into account (see Sect. 3), we continue to have more than 15 (more or less free) model parameters: 5 defining the geometry, 2 for the dynamics, 5 for the temperature, 3 for the density, and finally the $^{12}\text{CO}/^{13}\text{CO}/\text{C}^{17}\text{O}$ abundance ratio. It is difficult to decrease such a high number of parameters because of the different components identified in the maps: the hotter and less dense fringes separated from the equator, an outer less dense region, the cold central part of the disk, and the central hotter region.

On the other hand, our procedure allows an intuitive analysis of the relevance of the different parameters. We can infer that some parameters are not so relevant in fitting some observational properties, and that certain observational features are related to only one or two model parameters. For instance, the total size of the disk is selected to match the total extent of the image, which depends weakly on, e.g., the rotational velocity.

It has been argued that in sources comparable in angular size to the telescope resolution, the comparison performed in the image plane is inaccurate. This is untrue in our case, since GoHam occupies an area about 30 square arcseconds, almost a factor of 20 larger than the beam of our $^{12}\text{CO } J=2-1$ data. The cleaning process always introduces noise, but, besides numerical noise, it is mostly due to uncertainties in the calibration of the complex visibilities, i.e., the true beam shape not being exactly equal to the theoretical beam function (for the uv coverage of the observation). Subtraction of the convolved ‘clean components’ and the subsequent convolution to obtain the final image introduces then spurious features, mainly when the uv sampling is poor. However, such unavoidable uncertainties in the amplitude and phase calibration also appear if the fitting is performed in the uv plane, and the limitation in the dynamic range of the observations due to them applies to both the sky plane and the Fourier transformed plane. On the other hand, we also note that Fourier transformation of the predicted brightness (which must be calculated for a finite grid of points in space coordinates from the standard radiative transfer equation) also introduces numerical noise.

As we see below in actual cases, it is practically impossible to define a single best-fit model in our case, because of the complex data set and model. Instead, we adopt criteria to consider whether a set of parameter values is acceptable and, when they are not satisfied, provide limits to these values. This process will

only be detailed for the most representative parameters: radius and width of the disk, central mass (i.e., rotational velocity law), typical densities and temperatures. There is no significant differences among the acceptable models, both in their predictions and in values of the relevant disk properties; one of them was chosen as our best-fit model.

To select the acceptable models, we basically use the comparison of the predictions with the observations of the ^{12}CO and $^{13}\text{CO } J=2-1$ lines, in which S/N and the spatial and spectral resolutions are particularly high. We checked that the predictions for the $J=3-2$ lines are also satisfactory. The criteria used to select acceptable models are:

c1) The differential image, i.e., the difference between observed and synthetic velocity channels, must have, in the regions of each channel where emission is present, an *rms* noise not exceeding ~ 1.5 times that present in adjacent regions with no emission. Those regions, of noise not higher than 1.5 times that found in adjacent ones, are only slightly noticeable in the differential maps.

c2) In the differential $J=2-1$ image, the residuals must be smaller than 2 times the spurious contours (due to noise) seen in adjacent regions (~ 0.6 Jy/beam, two contours, in our $^{12}\text{CO } J=2-1$ images), and no residual ≥ 0.3 Jy/beam must appear systematically, i.e., in the same spatial offsets for several velocity channels. We note that one can identify noise features more intense than 0.3 Jy/beam in the observed $^{12}\text{CO } J=2-1$ maps, so residuals not exceeding the above limits are again not clearly different than the observation noise.

These conditions are relaxed for velocities around $4.5-5.5 \text{ km s}^{-1}$ LSR, which present a strong emission clump with no counterpart in the equivalent blue-shifted emission. This excess cannot be due to opacity or excitation effects, since it is more prominent in the $^{13}\text{CO } J=2-1$ maps than in the $^{12}\text{CO } J=2-1$ ones and much more than for $^{12}\text{CO } J=3-2$. The excess is also clear in the $\text{C}^{17}\text{O } J=3-2$ maps. The fact that this excess is so remarkable in the less optically thick ^{13}CO emission strongly suggests that it is mainly due to the presence of a gas condensation, rotating at about 2.5 km s^{-1} at a distance of about $5 \times 10^{15} \text{ cm}$ from the star. Our model shows axial symmetry and therefore cannot explain this excess; we chose to fit mainly the emission from the rest of the nebula. A tentative model fitting of this feature is presented in A.3, and the consequences and possible origins of the presence of this condensation are discussed in Sect. 4.1.

In Fig. A.1, we present the residuals of our fitting of the $^{12}\text{CO } J=2-1$ maps. Predictions and residuals for $^{13}\text{CO } J=2-1$ are shown in Figs. A.2 and A.3. Except for the velocities around 5 km s^{-1} , the typical *rms* noise outside the emitting regions is about 0.1–0.11 Jy/beam (slightly less for $^{13}\text{CO } J=2-1$), and does not exceed 1.5–1.7 Jy/beam in the regions with emission. We see that the largest residuals in the differential images do not reach two contours (noise reaching one level is also seen out of the emitting regions).

Of course, between 4.5 and 5.5 km s^{-1} , the situation is worse, reflecting the asymmetry in the disk density mentioned above. We can notice some other minor features in the images that are not accounted for by our model. For instance, the ^{13}CO line emission at 3.7 km s^{-1} is less extended than expected, which is not the case at 4.1 km s^{-1} . We also note in our ^{13}CO maps a weak extent towards the north at about 1.3 km s^{-1} , but practically at the noise level. In $^{12}\text{CO } J=2-1$, we see a similar protrusion, but not exactly at the same position. We finally note in some observed panels that the emission from regions close to the star (see, e.g., the $^{13}\text{CO } J=2-1$ emission at $\sim 0.5 \text{ km s}^{-1}$ and the

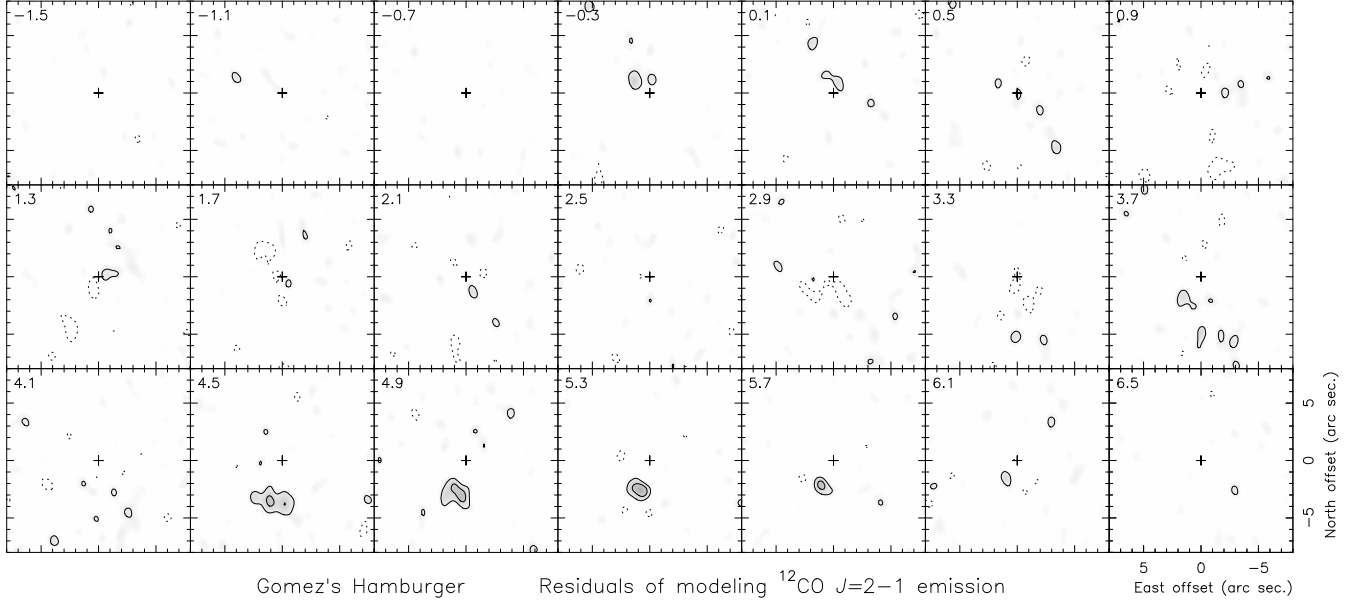


Fig. A.1. Residuals (observations minus synthetic maps) of the $^{12}\text{CO } J=2-1$ line brightness from our best model fitting for the GoHam disk. The spatial scale and contours are the same as in the observations and predictions, Figs. 1, 6.

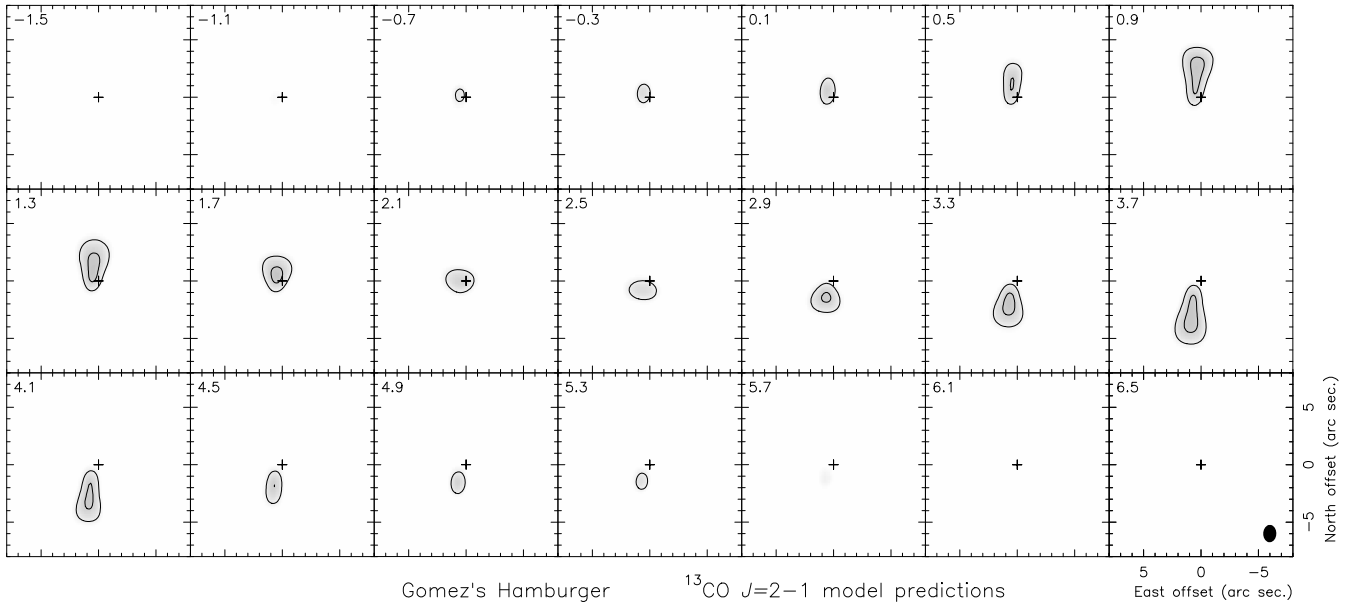


Fig. A.2. Predictions of the $^{13}\text{CO } J=2-1$ line brightness from our best model fitting for the GoHam disk. The spatial scale and contours are the same as in the observations, Fig. 2.

Table A.1. Relative range of acceptable values, around those given in Table 1, of the main parameters defining the model disk in Gomez's Hamburger.

Representative parameter	Acceptable range	Comments
Disk radius	$\times/\div 1.1$	R_{out} and R_{m}
Disk width	$\times/\div 1.1$	H
Keplerian velocity	$\times/\div 1.1$	V_l
Temperature	$\times/\div 1.1$	characteristic value
High- z jump	between 2 and 5	depends on calibration, possible exc. effects (see A.2)
Density	$\times/\div 1.5$	characteristic value
Outer disk density	$\times/\div 3$	only given by ^{12}CO data, possible exc. effects (A.2)
Turbulent velocity	$\leq 0.1 \text{ km s}^{-1}$	local velocity dispersion
$X(^{12}\text{CO})/X(^{13}\text{CO})$ rel. abundance	$\times/\div 1.5$	
$X(^{12}\text{CO})/X(\text{C}^{17}\text{O})$ rel. abundance	$\times/\div 2$	

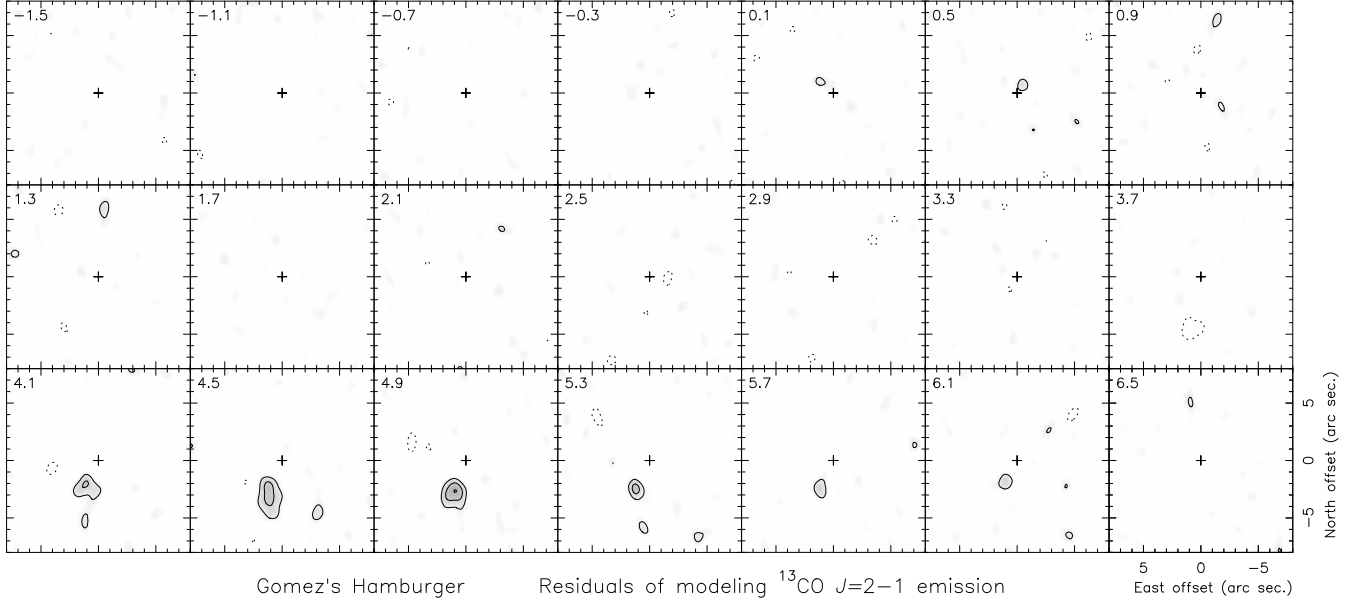


Fig. A.3. Residuals (observations minus synthetic maps) of the $^{13}\text{CO } J=2-1$ line brightness from our best model fitting for the GoHam disk. The spatial scale and contours are the same as in the observations and predictions, Figs. 2, A.2.

^{12}CO emission at 3.7 km s^{-1}) is more extended than the predictions. The width of our disk is given mainly by the equation of hydrostatics (Sect. 3), under the standard theory of massive flaring disks; it is possible that these usual theoretical requirements are not fully satisfied in the innermost regions of the disks, although further analysis of this phenomenon obviously requires higher-quality observations.

A.2. Uncertainty in the fitted parameters

We estimated the uncertainties in derived values of the model parameters by varying the values of each one (while the others remain unchanged) and checking the values for which the above conditions, **c1** and **c2**, were clearly not satisfied. This procedure was completed for the main, most representative parameters, for instance, the disk radius R_{out} , the characteristic density, etc. The results are summarized in Table 1. We also present below some cases in which the uncertainty in the derived parameters requires some discussion.

We did not attempt to consider fully the parameter uncertainties when two or more parameters are allowed to vary. For example, the density range is slightly larger than that given in the table if we allow the temperature also to vary, since both variations are in some way compensated. In general, however, the ranges do not differ very much from our standard uncertainty brackets. The density is mostly fixed by the emission of ^{13}CO and that of $^{12}\text{CO } J=2-1$ from outer regions, while the temperature law is mainly given by the $^{12}\text{CO } J=2-1$ and $J=3-2$ maps.

We note the uncertain determination of the density in the outer disk ($r \sim R_{\text{out}}$), which is only given by the ^{12}CO emission, since ^{13}CO is not detected in this region (see Table A.1). We also recall that the assumption of level population thermalization may be invalid for these diffuse regions, which may imply that the density in them is higher than the values given here, perhaps closer to $3 \times 10^3 \text{ cm}^{-3}$.

Important problems with the thermalization assumption are unexpected for the relatively high densities of the remaining nebula and the analyzed transitions (Sect. 3). The $J=6-5$ transition is significantly more sensitive to these effects, due to the

relatively high Einstein coefficients of high- J transitions. We also expect underpopulation of the $J=6$ and $J=5$ levels in the high- z low-density regions, with $n \sim 10^4 \text{ cm}^{-3}$, leading to 6–5 brightness temperatures of under 10 K. This line would mainly come from this high temperature surface, and we think that this phenomenon is responsible for the non-detection of $^{12}\text{CO } J=6-5$ in our observations. Any further discussion is impossible because of the lack of accurate information about the $J=6-5$ emission. This relative underpopulation of high- J levels in the layers at high absolute values of z may lead to a relative overpopulation of the $J=2$ level, and therefore to more emission than expected in $J=2-1$. This effect could lead to slightly smaller jumps of the temperature, perhaps closer to factor 2.

Some parameter pairs are quite dependent each on other. This is particularly true for the density and CO total abundance, since we assume LTE and then the line opacity depends on the product of the density and the relative abundance. Both parameters can therefore vary freely, provided that their product remains constant. The indetermination is solved assuming a relative ^{12}CO abundance of 10^{-4} . This is also the case for parameters that we have not considered separately in this uncertainty analysis, such as the temperature at a given point, $T(R_0)$, and the slope of the temperature law, α_T ; instead, as mentioned, we discuss the uncertainty in the characteristic temperature. Finally, we note the case of the rotation velocity and the conditions in the hot and dense center of the disk. Strong emission from these regions could mimic the emission of a faster rotating disk in the extreme velocity channels. So, the rotation velocity is mainly determined from the emission extent in the channels at moderate velocities, the emission at the extreme channels depending on both the Keplerian velocity and the emissivity of the central regions. In general, the uncertainty in the parameters defining the inner, denser region ($r < 2 \times R_{\text{in}}$) is high, because this clump is not resolved and the number of independent observational constraints is small (as also concluded in Paper I). We can say that an inner region of higher density and temperature is necessary to attain our strong requirements on the fitting quality and that it must be smaller than about 10^{16} cm , but we cannot provide details of this region.

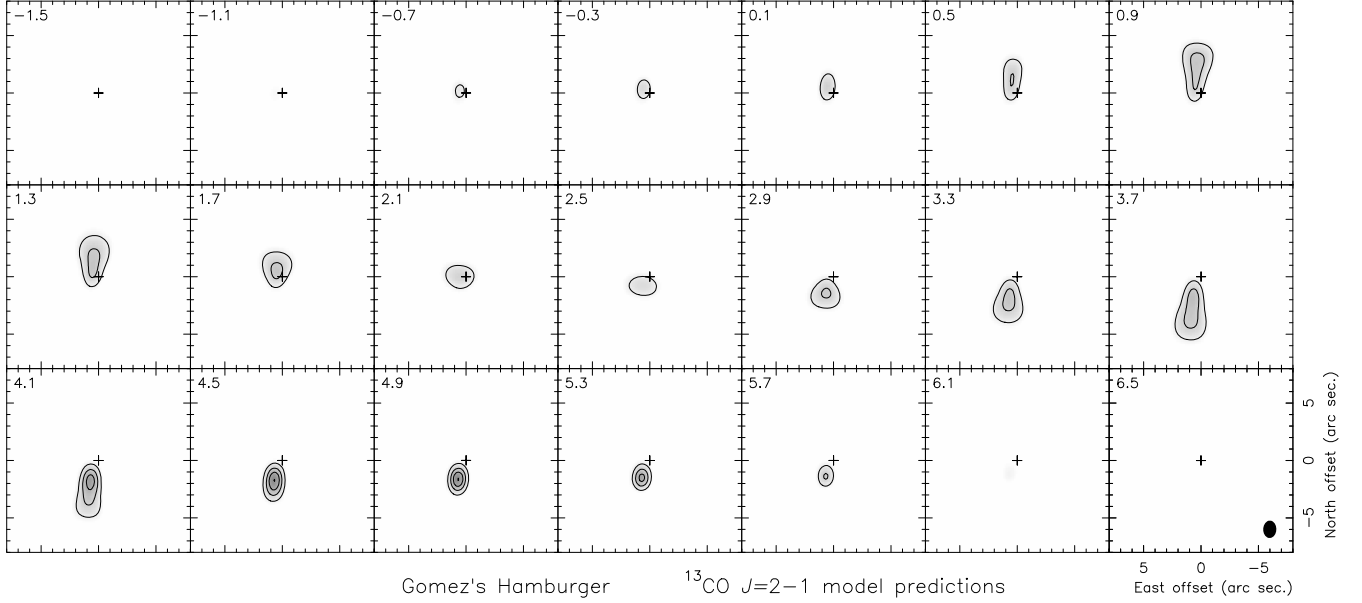


Fig. A.4. Predictions of the $^{13}\text{CO } J=2-1$ line brightness from our best model fitting for the GoHam disk, including the increase in temperature and density in a southern clump, as described in Appendix A.3. The spatial scale and contours are the same as in the observations, Fig. 2, and our standard model predictions, Fig. A.2.

The outer hot region, for high values of z , is hardly resolved in our ^{12}CO maps. Therefore, we could also reproduce our data assuming that this region is significantly thinner and brighter (in general, hotter) than in our standard model. However, those disk models are less probable than our standard one, since the jump in temperature we found is already quite high (see Sect. 3). Moreover, for very high temperatures in the high- z rim, we should also increase the typical density significantly (to be able to reproduce $^{12}\text{CO } J=2-1$ data, which, for the assumed dependence of density on z , is only moderately opaque in the high- z regions). This would then imply too low values of $X(^{13}\text{CO})$, when attempting to reproduce the $^{13}\text{CO } J=2-1$ data, leading to improbably high values of $X(^{12}\text{CO})/X(^{13}\text{CO})$, of significantly over 100. In any case, we note that the properties of this high- z bright rim depend on the relative calibration of the $J=2-1$ and $J=3-2$ lines; allowing 15% variations in the relative calibrations, we can fit the data with temperature jumps ranging between 2 and 5 (and hot-layer widths that do not differ significantly from our standard value).

A.3. Model (tentative) fitting of the southern brightness maximum

We mentioned that there is a relative maximum in the southern part of the disk that has no counterpart in the north. This maximum is seen in all our maps, but is more prominent in the ^{13}CO emission, which is mostly optically thin, as well as in the C^{17}O line. Therefore, this brightness maximum must be due mainly to an increase in the density of some southern regions, although an increase in temperature is also necessary to explain the excess observed in $^{12}\text{CO } J=2-1$.

In our standard model analysis, we mostly tried to fit the emission from the rest of the nebula (Sects. 3, A1, A2). Any attempt to fit the emission excess from this southern clump is very uncertain, because of the lack of previous experience in trying to study condensations of this kind, including the lack of theoretical modeling, and because of the poor information contained in our observations, which scarcely resolve its extent.

Nevertheless, we note that this emission excess can be detected over a remarkable range of velocities, between about 4.1 and 5.7 km s^{-1} LSR. This means that the emitting condensation cannot be very small, the projected velocity dispersion being caused by gas emission from different distances from the star or from regions showing a significant variation in the velocity projection along the line of sight. In both cases, we expect typical sizes $\sim 5 \times 10^{15}$ cm ($\sim 1''$ for the adopted distance). We can also assume that the condensation occurs in the equatorial disk regions in which $^{13}\text{CO } J=2-1$ emission originates, because the maximum is so prominent in this line. We have assumed that the emission comes from a region defined by $R_{\text{in}} < r < 10^{16}$ cm, and $z_s/r < 0.6$, where z_s is the distance between a given point and the plane containing the star and perpendicular to the equator that gives the extreme projections for the rotation velocity. We assume that the temperature and density of this region vary with respect to the standard laws assumed for the rest of the nebula.

To explain the (moderate) emission excess found in $^{12}\text{CO } J=2-1$, we estimate that we must assume an increase in temperature in the southern condensation of a factor ~ 1.5 , with respect to our standard laws for nearby regions. Finally, we estimate the excess density in the condensation by comparing the model results with the intensity of $^{13}\text{CO } J=2-1$. Since the $^{13}\text{CO } J=2-1$ emission from these inner regions is not fully optically thin and the beam dilution is not negligible, a significant density increase, of a factor 10, is necessary. A total mass increase of about $6 \times 10^{-3} M_{\odot}$ is deduced.

The resulting brightness distribution is shown in Fig. A.4. We can see that the brightness excess of $^{13}\text{CO } J=2-1$ in this southern clump is reasonably well reproduced, but the location of the predicted maximum is slightly closer to the star than the observed one. This cannot be avoided assuming a larger distance from the star for the clump, because then the velocity of the feature would be less positive. The velocity field in this region must then also be disturbed. See discussion on the interpretation of this emission excess in Sect. 4.1.